Thermodynamic stability of β-phases in Zr-Nb alloys

Vidur Tuli[*] and Patrick Burr

School of Mechanical and Manufacturing Engineering, University of New South Wales, Kensington NSW 2033, Australia

Antoine Claisse

Westinghouse Electric Sweden, Västerås SE 72163, Sweden

Claudio Cazorla

Department of Physics, Universitat Politècnica de Catalunya (UPC), Barcelona, Catalonia B4-203, Spain

We investigate the contribution of mixing enthalpy, configurational entropy, vibrational entropy, and electronic entropy towards the thermodynamic stability of β-(Zr,Nb) phases, to explain discrepancies in experimental observation of irradiated Zr-Nb alloys. Mixing enthalpy, configurational entropy, and electronic free energy alone are insufficient to explain the relative stability of these phases. This emphasises the need for accurate determination of the vibrational free energy contributions, which we calculated using *ab initio* molecular dynamics. Including vibrational free energy contributions predicts β-Zr decomposition in to HCP-Zr and β-Nb at temperatures below $\sim$880 K, in line with experimental observations. The relative energy difference between β-Zr decomposition between 600 and 1200 K is small ($<$0.1 eV/atom) and may explain the wide range of apparently stable β phases observed in neutron and proton irradiated Zr-Nb alloys. Other factors that may contribute towards the stability of these phases are also discussed.

I. INTRODUCTION

Zr-Nb alloys with 0.5–2.5 wt% ($\sim$0.49–2.45 at.%) Nb are used as nuclear fuel cladding in nuclear reactors due to a combination of favorable neutronic, mechanical, and corrosion properties [1–3]. Nb alloying addition provides improved oxidation and hydrogen-pickup resistance. Nb-containing Zr alloys include Zirlo$^{\mathrm{TM}}$($\sim$1 wt% Nb) [2], M5 ($\sim$1 wt% Nb) [3], Zr-1%Nb, Zr-1.5%Nb, and Zr-2.5%Nb. Depending on the processing conditions and the irradiation conditions, Nb can be accommodated in a range of different phases with conflicting reports in the literature, suggesting that the thermodynamics of these competing phases are not yet fully understood.

Figure 1 shows the Zr-Nb phase diagram from literature [4,5]. In all Zr alloys, Nb is soluble in the α phase, and when added above its solubility limit ($\sim$0.4 wt%), Nb precipitates into β-Nb particles [6–9], which are β-(Zr,Nb) solid solutions with up to 90 wt% Nb [8,9]. In alloys annealed at higher temperatures, e.g., Zr-2.5%Nb, the metastable β-Zr phase (50–80 wt% Zr) forms due to alloy annealing above the monotectoid temperature of 610 °C [10,11]. The metastable β-Zr phase is also present in Zr-1.0%Nb, Zr-1.5%Nb, and Zr-2.0%Nb alloys annealed at 640 °C, which is above the monotectoid temperature [12]. The β-Zr phase can be retained at low temperatures as a metastable phase, but heat treatment under the monotectoid temperature decomposes in to either ω phase or β-Nb with heat treatment below 530 °C [13,14].

The Nb content in the β-Nb phase is reported to reduce with exposure to neutron and ion irradiation, to varying levels based on the irradiation conditions. Reduction up to 55–60 wt% Nb is reported under neutron irradiation in M5 alloys up to 22 dpa [9]. In Zr-1.5%Nb alloy, a reduction to 82.83 wt% is reported with dpa level of 2.66 [15]. In Zr-1%Nb alloy, reduction to 50 wt% Nb under neutron irradiation is reported at 8.5 dpa [16]. In low-Sn Zirlo, proton irradiation causing 2.3 dpa reduced the Nb content in the native β-Nb precipitates to 40% [17].

A third Nb-containing phase has also been reported in Zr alloys exposed to neutron or proton irradiation. These irradiation-induced precipitates are nm-sized and have a platelet morphology. In-reactor neutron irradiation ($>$1 MeV at 350 °C and fluence of 1.1×10^{26} nm^{-2}) in M5 at damage level of 22 dpa induce Nb-rich precipitates containing up to 60 at.% Nb [18]. These precipitates have also been observed for dpa levels ranging from 4–22 dpa in similar in-reactor irradiation [9]. Similar precipitates have also been observed during in-reactor irradiation of Zr-2.5%Nb alloys [19]. The similar composition observed between post irradiation native β-Nb particle and platelet-like precipitates at high fluences is considered to be the equilibrium concentration of these particles under irradiation, which is different than the thermodynamic equilibrium at similar temperatures. This is due to the change in solubility caused by irradiation-enhanced diffusion controlled by migration of nonequilibrium irradiation-induced point defects [20,21]. On the other hand, proton irradiation (2 MeV at 350 °C, up to 1 dpa, flux of 3.67×10^{13} ion/cm^2 s and dpa rate 2.62×10^{-6} dpa/s) is reported to induce precipitates only containing 10–40 at.%

————
[*]vidur.tuli@unsw.edu.au
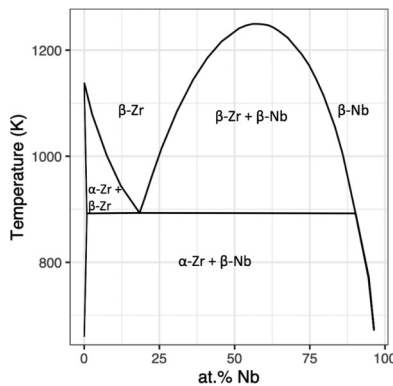
FIG. 1. Zr-Nb phase diagram. Modified from [4,5].

Nb [22,23], and larger in size (20–100 nm vs 2–10 nm in length).

Even though such a wide range of β phases have been observed in Zr-Nb alloys, there is a lack of fundamental understanding of the thermodynamics of the β-(Zr,Nb) system. The fact that a variety of phases have been reported under relatively similar conditions suggests that the stability of these phases may be dictated by small differences in energies governing the relative stability of these phases. This requires complex modeling approaches to obtain accurate and precise thermodynamic information. Previous studies on the thermodynamic stability of β-(Zr,Nb) solid solutions have either not included vibrational free energies or have only considered harmonic approximations towards vibrational frequencies [24,25]. BCC-Zr is known to be strongly anharmonic [26,27]. This creates a challenge when calculating the vibrational free energy contributions towards pure BCC-Zr or Zr-rich BCC solid solutions at finite temperatures as the stabilizing effects of anharmonic vibrations cannot be ignored. *Ab initio* molecular dynamics has been shown to accurately capture the anharmonic vibrational frequencies of a wide range of metals and intermetallics [28–31]. A previous study done on the β-(Zr,Nb) system has resorted to an extension to the ground-state theory—density functional perturbation theory (DFPT), which only considers harmonic approximations to the vibrational frequencies. It has been shown that DFPT may not be efficient in capturing anharmonic effects in systems with strong anharmonicity, leading to the need to explicitly model Zr-rich BCC solid solutions at high temperatures [24].

Previous studies have used atomic scale simulations to accurately capture the individual contributions towards Gibbs free energy of formation of a range of systems. For instance, the study by Hossain *et al.* showed that single-phase rock salt structured high-entropy carbides are thermodynamically stable above 3000 K with configurational entropy contribution being two orders of magnitude larger than the electronic and vibrational entropies [32]. The study by Manzoor *et al.* on a range of high-entropy alloys showed that relying solely on enthalpy of mixing enthalpy may not lead to correct phase stability predictions and including entropy contributions are critical for accurate predictions [33]. The study by Fan *et al.* used atomic scale simulations to show that in addition to just the mixing enthalpy, accurate electronic, vibrational, and

magnetic entropy contributions are important to explain the Fe-Y phase diagram [34]. Atomic scale calculations have also been used to compute the Gibbs free energy of iron-based binary alloys, providing insights into phase transitions under different conditions [35,36]. These examples highlight the importance of atomic scale calculations in accurately calculating the Gibbs free energy contributions, providing valuable insights for materials science and engineering. Here we explore the thermodynamics of the β-(Zr,Nb) system, to quantify the contributions from mixing enthalpy, configurational entropy, electronic free energy, and vibrational free energy.

II. METHODS

This study involved calculating the free energy of formation of β-(Zr,Nb) phase containing 0, 25, 75, and 100 at.% Nb. The 25 and 75 at.% Nb compositions were selected to represent β-Zr and β-Nb phase, respectively. The relative stability of the two β phases were calculated considering the β-Zr decomposition reaction

$$\beta\text{-Zr} \longrightarrow \text{HCP-Zr} + \beta\text{-Nb}, \tag{1}$$
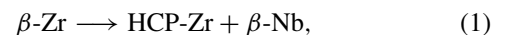
where the Gibbs free energy of the reaction (ΔG) was calculated as

$$\Delta G(T) = G_{\text{HCP-Zr}} + G_{\beta\text{-Nb}} - G_{\beta\text{-Zr}}. \tag{2}$$

The Gibbs free energy is the fundamental driving force behind the phase formation reaction, and is defined as

$$G(T) = U + PV - TS, \tag{3}$$

where U is the internal energy, P is the pressure, V is the volume, T is the temperature, and S is entropy. U and S in Eq. (3) can be approximated by their key components

$$G(T) = (U_{\text{DFT}} + U_{\text{elec}} + U_{\text{vib}}) + PV$$
$$- T(S_{\text{conf}} + S_{\text{elec}} + S_{\text{vib}}), \tag{4}$$

where the subscripts vib, elec, and conf stand for vibrational, electronic, and configurational respectively. It is worth noting that the translational and rotational free energies have been ignored as they are expected to have really small contributions towards G in solid-state phases. The contribution of creating an interface with the bulk of the alloy was out of scope for this study, as we aim to study the fundamental thermodynamics of the Zr-Nb system.

Equation (4) can also be written as

$$G(T) = U_{\text{DFT}} + PV - TS_{\text{conf}} + F_{\text{elec}}(T) + F_{\text{vib}}(T), \tag{5}$$

where F_{vib} and F_{elec} are the Helmholtz vibrational and electronic free energies.

HCP-Zr was modelled as a pure Zr cell, while β-Zr and β-Nb were modelled as disordered solid solutions using two approaches: special quasirandom structures (SQS) and configurational ensemble. SQS structures represent the features of an ideal solution with maximal disorder, thus it is appropriate to assume maximum configurational entropy, S_{conf} (i.e., ideal gas) in the absence of exact configurational entropy information. This can be calculated using the Stirling's approximation [37]

$$S_{\text{conf}} = -R(x_{\text{Zr}}\ln x_{\text{Zr}} + x_{\text{Nb}}\ln x_{\text{Nb}}), \tag{6}$$

where R is the gas constant and x is the fraction of solute in β-(Zr,Nb) solid solution. The toolkit used to generate the SQS structures was the MCSQS code in the alloy theoretic automated toolkit (ATAT) developed by Van de Walle *et al.* [38]. On the other hand the configurational ensemble approach provides exact configurational entropy information of the simulated ensemble. The tool used for the implementation of configurational ensemble is the site-occupancy disorder (SOD) code developed by Grau-Crespo *et al.* [39]. The SOD approach considers all possible configurations at each composition, while exploiting the space group operations to reduce the configurational space to symmetry-unique sets. The probability (P_n) of each symmetrically distinct configuration to exist is calculated as

$$P_m = \frac{1}{Z}\Omega_m e^{\frac{-E_m}{k_B T}},\tag{7}$$

where the E_m and Ω_m are the reduced energy and degeneracy information of each configuration respectively. Z is the partition function defined as

$$Z = \sum_{m=1}^{M}\Omega_m e^{\frac{-E_m}{k_B T}}.\tag{8}$$

The SOD approach also allows us to calculate the configurational average of physical properties of the ensemble such as configurational entropy (S_{conf}) of the system

$$S_{\text{conf}} = \frac{(\sum_{m=1}^{M}E_m P_m) - (-k_B T \ln Z)}{T}.\tag{9}$$

Three SQS were created per composition, using 128 atom supercells with interactions considered up to the third-nearest neighbors and the SOD structures contained 16 atoms. Pure BCC-Nb and BCC-Zr were represented by 120 atom supercells, while HCP-Zr was represented by a 150 atoms supercell. These structures were fully relaxed using DFT simulations carried out using the VASP code [40,41] with the PBE exchange correlation functional, a consistent plane wave cut off energy of 350 eV. Atoms were described with PAW pseudopotentials from the VASP 5.4 repository. Partial occupancy were treated with a first-order Methfessel-Paxton smearing function of width 0.1 eV.

The mixing enthalpy ΔU_{mix} of disordered structures (solid solutions) was calculated as

$$\Delta U_{\text{mix}} = U_{\text{DFT}}^{\text{ss}} - x_{\text{Zr}}U_{\text{DFT}}^{\text{BCC-Zr}} - x_{\text{Nb}}U_{\text{DFT}}^{\text{BCC-Nb}},\tag{10}$$

where ss signifies solid solution made up of BCC-Zr and BCC-Nb. U_{DFT} signifies the DFT energies and all supercells contain equal number of atoms to ensure mass balance. The formation enthalpy ΔU_{f} was calculated with respect to BCC-Nb and HCP-Zr as HCP-Zr is the ground-state allotrope of Zr,

$$\Delta U_{\text{f}} = U_{\text{DFT}}^{\text{ss}} - x_{\text{Zr}}U_{\text{DFT}}^{\text{HCP-Zr}} - x_{\text{Nb}}U_{\text{DFT}}^{\text{BCC-Nb}}.\tag{11}$$

The electronic free energy was calculated from single-point energy calculations of the relaxed HCP-Zr, BCC-Nb, and SQS structures representative of β-(Zr,Nb) phases. In these simulations the electronic bands were smeared with a Fermi distribution of width $k_B T$, and all other parameters were kept the same as above.

The vibrational free energy was calculated by integrating the vibrational density of states [$g(\omega)$], which was computed as the Fourier transform of the velocity autocorrelation function [$c(t)$] of *ab initio* molecular dynamics (AIMD) trajectories. $c(t)$ is a time-dependent correlation function that relates the velocity of an atom j at time t to its initial velocity and is calculated as a scalar product, which is averaged over the number of particles

$$c(t) = \frac{1}{N}\sum_{j=1}^{N}\langle v_j(t) \cdot v_j(0)\rangle.\tag{12}$$

$c(t)$ from all simulations were calculated as a mean of individual VACFs from 5 ps segments of the entire simulation length. The first segment was from the first step to the 2500th step, and each subsequent segment starts one step after the start of the previous segment. This results in 7500 sections of 5 ps in a 20-ps run. This increases the precision of the $c(t)$ with the amount of data available by mitigating the impact of random noise and short-term fluctuations.

The Fourier transform of velocity autocorrelation function of particle j, $c_j(t)$, gives us the power spectrum $|v_j(\omega)|^2$ [42]. We know that c_j is an even function, therefore only the real part of the FFT calculated using the equation below was considered

$$|v_j(\omega)|^2 = \int_{-\infty}^{\infty}c_j(t)e^{-j\omega t}dt.\tag{13}$$

Finally, $g(\omega)$ over N particles is directly proportional to the power spectra

$$g(\omega) = \frac{1}{3N}\sum_{j=1}^{N}|v_j(\omega)|^2.\tag{14}$$

Now if all atoms are considered as independent simple harmonic oscillators, the temperature-dependent Helmholtz free energy of an atom can be calculated as a one dimensional quantum harmonic oscillator

$$F_{\text{qm}}(T) = \frac{\hbar\omega}{2} + k_B T \ln(1 - e^{\frac{-\hbar\omega}{k_B T}}),\tag{15}$$

where $\hbar$ is the Planck's constant and $\frac{\hbar\omega}{2}$ is quantum zero-point energy, which is due to Heisenberg's uncertainty principle and increases the classically derived ground-state energy. Now, if all atoms are considered to be coupled harmonic oscillators, we can approximate the Helmholtz vibrational free energy (F_{vib}) of the system by summing over all wave vectors in three dimensions [43,44]

$$F_{\text{vib}}(T) = 3 \times \int_0^{\infty}g(\omega)F_{\text{qm}}d\omega,\tag{16}$$

where $g(\omega)$ is normalized such that the area under the DOS is 1. F_{vib} was calculated for all 7500 segments used for $c(t)$ calculations. The mean values and standard deviations of F_{vib} have been reported in the Sec. III.

AIMD simulations to obtain vibrational free energy were used for the stability analysis of β-(Zr,Nb) phases containing 0, 25, 75, and 100% Nb. The analysis was limited to these two solid solution compositions because they are closest to the experimentally observed β-phase compositions. Additionally,
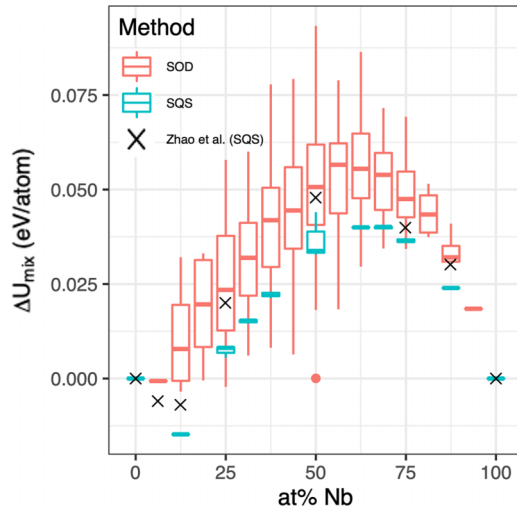
FIG. 2. ΔU_{mix} of β-(Zr,Nb) calculated with respect to BCC-Zr and BCC-Nb. The bar represents the median ΔU_{mix} value and the width of the box represents the Q1–Q3 interquartile range. The whiskers represent the 95% confidence interval and the point represents outlier. Also shown are the ΔU_{mix} values from literature calculated using DFT energies of a single-SQS structure per composition [25].

the mixing enthalpy results shown in Fig. 2 indicate that the 50 at.% Nb solid solution is least likely to exist and DFT energies obtained at high Zr concentrations are unreliable due to dynamic instabilities of the β-(Zr,Nb) system at 0 K. 25 and 75 at.% Nb structures were created as special quasirandom structures. The simulation length was set at 20 ps with 2-fs time steps. Gamma-point only version of VASP was used to run these simulations. Single-k point (Γ) provides a reasonable compromise of accurate forces and simulation length [45,46]. All structures for AIMD were $3 \times 4 \times 5$ supercells containing 120 atoms. The choice of $3 \times 4 \times 5$ supercell is based on the sensitivity analysis presented in the Supplemental Material [47], and was found to provide a good balance between computational requirements and accuracy. In particular, anisotropic supercells were found to capture long range effects more efficiently that isotropic supercells, in agreement with previous reports [48].

The volume corresponding to zero pressure was found with a linear regression between volumes and pressures at each temperature. While the pressure-volume relationship is known to a quadratic function, a linear approximation is valid in a region of small change in volume [49]. Three volumes were simulated for all compositions at 600 K and 1200 K, except for BCC-Nb, where four volumes were simulated.

The linear regression between Helmholtz free energy and volume is calculated by taking a weighted linear fit (weighting factor is inversely proportional of standard deviation of Helmholtz energies at all volumes) between the energy and volumes. Zero-pressure F_{vib} is obtained as per

$$F_{\text{vib}} = mV_0 + c, \tag{17}$$

where, m and c represent the slope and intercept of the weighted linear regression, and V_0 represents the zero-pressure volume. The residual standard error (ϵ), which

represents the error bars is given by

$$\epsilon = \sqrt{\frac{\sum_{i=1}^{n}(F_{\text{vib}} - \hat{F}_{\text{vib}})}{n-2}}, \tag{18}$$

where, the numerator signifies the difference between the actual and predicted value (linear fit value) of vibrational free energy at same volume. n signifies the number of data points provided to calculate the linear fit.

III. RESULTS

A. Internal energy of mixing, configurational entropy, and electronic free energy

ΔU_{mix} of the β-phase formation reaction was calculated using the difference between DFT energies of the product [β-(Zr,Nb)] and the reactants (BCC-Zr and BCC-Nb). Here we consider the two BCC end members instead of the ground-state HCP-Zr phase as we first present the mixing enthalpy as per the standard definition, which allows us to compare our results with available literature. The energy associated with the formation of β phase from the HCP allotrope is included later. Figure 2 shows the ΔU_{mix} contribution towards the formation free energy of the β-(Zr,Nb) phases from structures created using two methods—SQS [38] and SOD [39]. The overall positive energy values across the composition range indicate that, like most metals, a miscibility gap is expected at low temperatures and that entropy plays a crucial role in stabilizing the solid solution. Experimentally it has been shown that the ΔU_{mix} for Zr-Nb solid solutions is positive [50,51] and this positive ΔU_{mix} is also common for other metallic solid solutions [52,53]. We observe negative values for ΔU_{mix} at high Zr concentrations in the solid solution ($\sim$87.5 at.%), in agreement with previous reports [25,54]. This negative ΔU_{mix} may be due to the dynamic instability of the Zr-rich β-(Zr,Nb) system at 0 K, making the results somewhat unreliable as the simulation cells undergo displacive distortions during relaxation. Even though the SQS and SOD results were obtained using different approaches, we observe common trends in both set of results. Most of the SQS ΔU_{mix} values are also within the whiskers of SOD results; this is expected as the ensemble approach can describe all configurations between the full order and the full disorder limits, while the SQS method is designed to model an atomic configuration representative of complete disorder.

Figure 3 shows the contribution of configurational entropy towards the stability of β-(Zr,Nb). SQS calculations assume maximal configurational entropy, while SOD results include the exact configurational entropy of the ensemble. A considerable peak in energies is also observed for the SOD results at 50 at.% Nb composition at lower temperatures. This is due to the fact that at low temperatures the configurational average is dominated by the lowest energy configuration. As temperature increases, the configurational ensemble gets closer to ideal mixing (which is assumed in the SQS system) and the dip in energy is less pronounced. While the $T\Delta S_{\text{config}}$ values significantly reduce the free energy of the solid solutions, the values become commensurate with the ΔU_{mix} values only above 900 K. Moreover, the internal energy difference
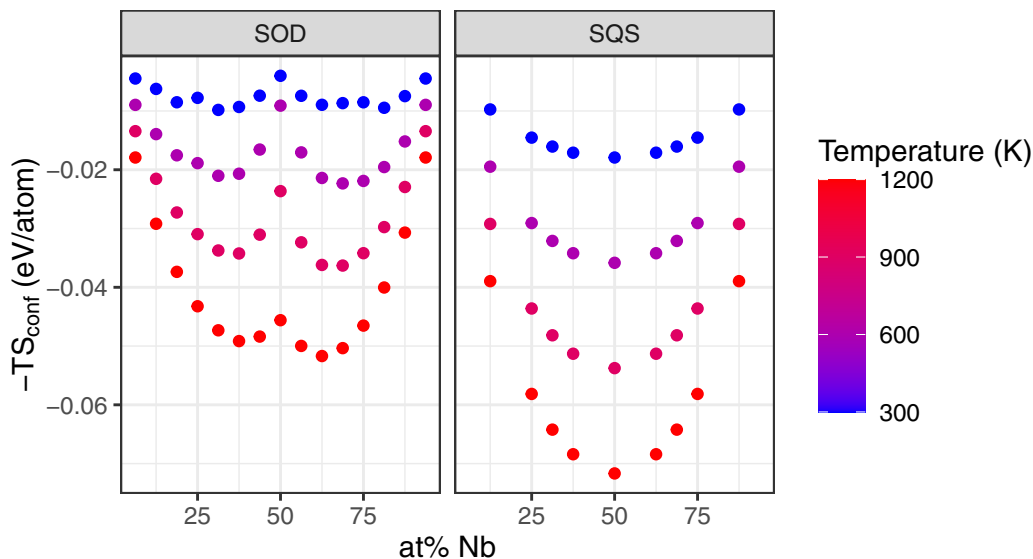
FIG. 3. $-TS_{\mathrm{conf}}$ contribution to stability of β-(Zr,Nb).

between HCP-Zr (ground-state allotrope of Zr) and BCC-Zr, $U_{\mathrm{HCP\text{-}Zr}} - U_{\mathrm{BCC\text{-}Zr}} = -0.085$ eV, further increases the value of ΔU_{mix}, thus mixing enthalpy and configurational entropy alone do not explain the experimental observation of β-Nb in Zr-Nb alloys below the solvus temperature.

Figure 4 shows the electronic free energy contributions towards the stability of β-(Zr,Nb). Electronic free energy contributions are of similar magnitude for both Zr-rich and Nb-rich phases, and increase with increasing temperature. Thus, adding the electronic free energy contributions to the formation enthalpy and configurational entropy contributions does not significantly affect the relative stability of β-Nb and β-Zr. Next we consider vibrational enthalpy and entropy contributions to the formation free energy.

B. Vibrational free energy

The vibrational free energy is calculated using AIMD. It is common to attain the vibrational free energy using lattice dynamics through DFT-based calculation of phonon dispersion relations within the QHA [55,56]. However, within this approach the main assumption that the potential energy surface expanded only up to second-order terms is temperature independent fails when anharmonic effects are important. This becomes a severe issue when applied to crystal structures that are dynamically unstable at 0 K [26]. This is illustrated in Fig. 5, which shows imaginary frequencies for the calculated $g(\omega)$ for β-(Zr,Nb) containing 87.5 at.% Zr calculated from DFT using the small displacement method [57]. The use of AIMD simulations to explicitly model materials at high temperature, introduces temperature and volume effects on phonon interactions. This overcomes the limitation of the traditional DFT-based approach. However, AIMD simulations

FIG. 4. F_{elec} contribution to stability of β-(Zr,Nb).
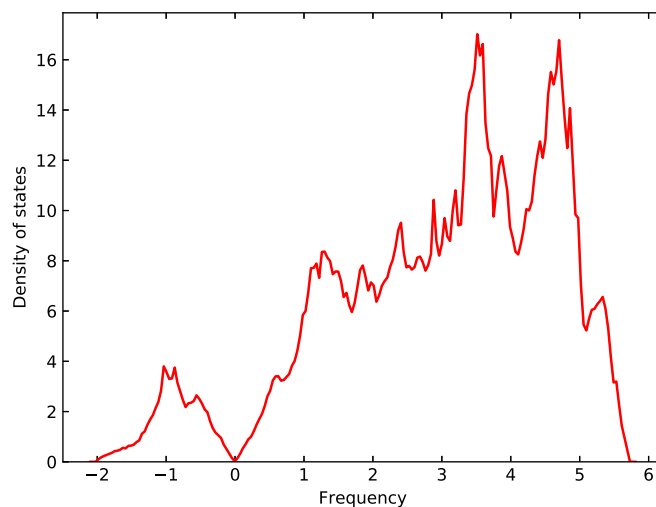
FIG. 5. $g(\omega)$ for (Zr,Nb) solid solution containing 87.5% Zr, obtained through DFT+QHA.
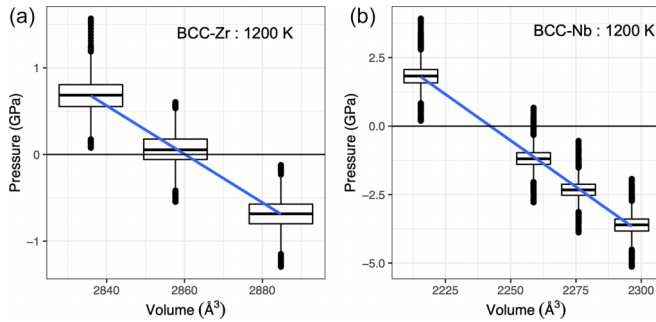
FIG. 6. Box and whiskers plot showing P-V relationship for (a) BCC-Zr and (b) BCC-Nb at 1200 K. Width of the box represents the Q1–Q3 interquartile range and points represent outliers.

are computationally expensive and require optimization of input parameters to reduce computational cost while accurately capturing the dynamics of the system. Some careful sensitivity analysis was required to ensure our AIMD simulations find a balance between computational time requirements and accuracy in capturing the vibrational dynamics of the system. Extensive simulation parameter convergence has been shown in the Supplemental Material [47].

The vibrational free energy was calculated from $g(\omega)$, which in turn was obtained from a Fourier transform of averaged $c(t)$ of AIMD simulations carried out in the NVT (canonical) ensemble with the Nose-Hoover thermostat [58]. The Nose-Hoover thermostat's inclusion of additional degrees of freedom that couple the system with the heat bath, avoids the random noise added to the results due to the stochastic nature of the Langevin thermostat (NpT ensemble). Since all simulations were carried out with the NVT ensemble, they were all at a nonzero-pressure state. Multiple AIMD simulations were carried out for each composition to identify the zero-pressure volume. Figure 6 shows the aggregate volume-pressure behavior for BCC-Zr and BCC-Nb simulations carried out at 1200 K. The results show a near-linear relationship, as expected by the P-V equation of state by Birch–Murnaghan and Rose-Vinet in the volume range of ~3% [49,59,60]. The linear fit is created with a confidence interval of 0.999 (the confidence interval is thinner than the linear thickness). This high quality of linear fit is due to the large number of points available at each pressure, with each set of data (box and whiskers) representing 10 000 AIMD data points (one pressure value at each time step) for each volume.

Similar trends were observed for the other compositions and temperatures simulated.

The lattice parameters of zero-pressure volumes for BCC-Zr and BCC-Nb are found by calculating the intercept of the linear fit line at zero pressure in the P-V relationships and are shown in Table I. The table also shows literature values for lattice parameters of BCC-Nb and BCC-Zr at 1200 K, which are in great agreement. Similarly, the lattice parameters for β-Zr (25 at.% Nb) phase and β-Nb (75 at.% Nb) phases are shown to follow Vegard's law of linear weighted average of the lattice parameter of the solid solutions' end members [61,62].

Figure 7 shows the pressure-temperature-energy relation for BCC-Zr and BCC-Nb at 600 and 1200 K. Interestingly in the case of BCC-Zr, analyzing the evolution of energy over the 20 ps run at 600 K showed possible transformation towards lower-energy structure. Interval common neighbor analysis [66], revealed that the structure distorted into a partly HCP configuration. As BCC-Zr is not stable at 600 K and ~500 MPa pressure, this provides confidence that the 20 ps AIMD simulations, with our carefully converged simulation parameters (see the Supplemental Material [47]), can capture the correct dynamics of the system. Due to this phase transformation, the results for BCC-Zr at 600 K were not considered for the purpose of this analysis. As expected, no such displacive transformation was observed at 1200 K. Further analysis of the 25 at.% Nb structures at 1200 K also confirmed that for all three volumes, the structure exhibits a quasi-BCC structure, where the average atomic position over several picoseconds result in a BCC structure. This is not abnormal behavior in MD for stable BCC structures, with similar structure previously observed for BCC-Zr simulated at 1000 K using classical MD [67].

Figure 8 shows the $g(\omega)$ as a function of composition, computed using the MD trajectories of the 1200 K simulations with volumes closest to the zero-pressure volume. Also shown is the partial vibrational density of states (pvDOS) contributions from Zr and Nb in the solid solutions. The pvDOS curves have been normalized by the atomic fraction of the species in the solid solution. The results show an increase in the phonon density at higher frequency with increasing Nb concentration. This is expected as with increasing Nb content the outer electrons per atom ratio increases resulting in stiffer bonds, and an increase in stiffness would result in higher phonon frequencies [68–71]. The pvDOS corresponding to both Zr and Nb have similar phonon distributions at the range of frequencies

TABLE I. Lattice parameters for BCC-Zr, BCC-Nb, and β-(Zr,Nb) solid solutions obtained from AIMD simulations.

at.% Nb	Temperature (K)	Simulated lattice parameters (Å)	Literature (Å)	Vegard's law (Å)
0	600	N/A		
0	1200	3.626	3.629 (exp.) [63]	
25	600	3.535		3.535
25	1200	3.553		3.555
75	600	3.392		3.397
75	1200	3.408		3.414
100	600	3.329		
100	1200	3.343	3.335 (AIMD) [64]	
100	295		3.320 (exp.) [65]	
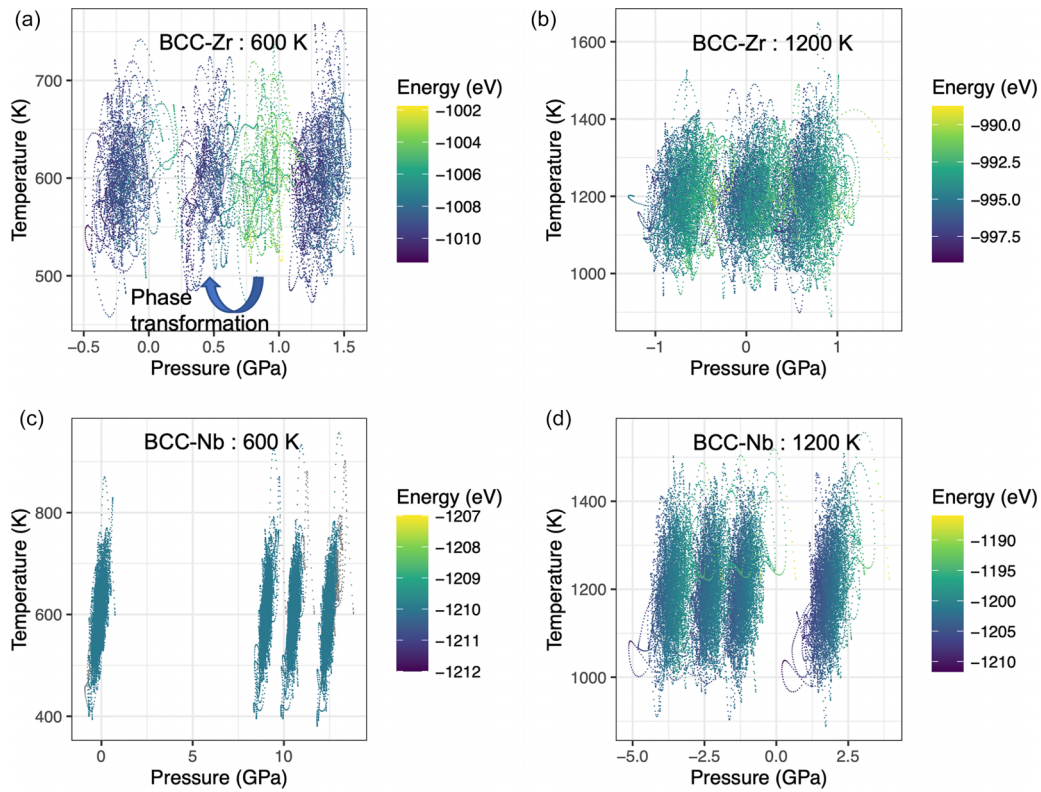
FIG. 7. Pressure-temperature-energy relations for BCC-Zr at (a) 600 K and (b) 1200 K and BCC-Nb at (c) 600 K and (d) 1200 K. Each point represents the pressure and energy at each step of AIMD simulation for all volumes over 20 ps.
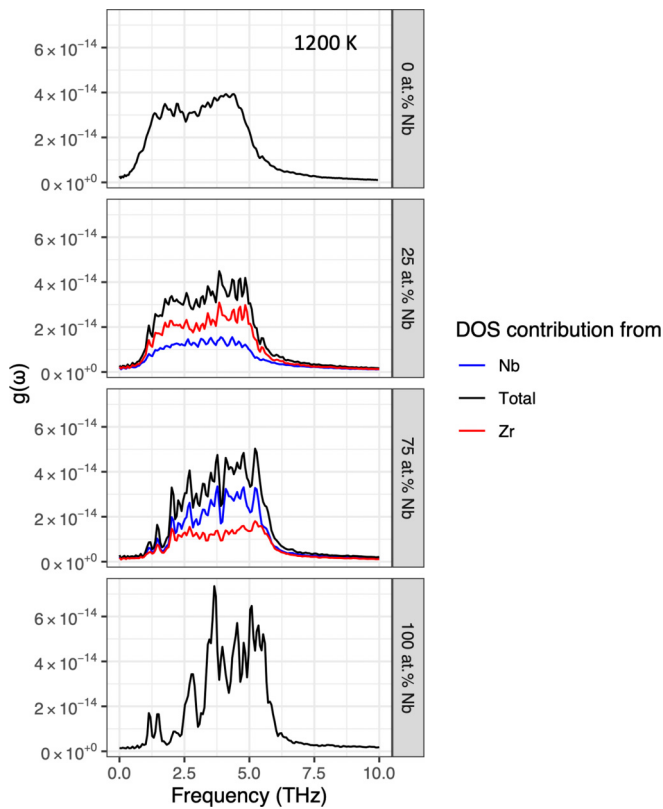
FIG. 8. $g(\omega)$ obtained from 20 ps AIMD runs for 0, 25, 75, and 100 at.% Nb at 1200 K.

probed, with peaks and valleys at similar frequencies, thus signifying similar lattice dynamics in both species.

Figure 9 shows the Helmholtz vibrational free energy F_{vib} obtained by integrating, at both 600 and 1200 K, the $g(\omega)$ obtained using the 600 K and 1200 K AIMD simulations of 75 at.% Nb structure. Similar trends were also observed for 25 at.% Nb and 100 at.% Nb. Integrating the $g(\omega)$ obtained from AIMD trajectories with ensemble temperatures of 600 K or 1200 K yielded equivalent F_{vib} values. This suggests that the difference in $g(\omega)$ between 600 K and 1200 K is negligible, at least in the frequency range relevant to the integrating temperatures, provided that the structure is stable at that tem-
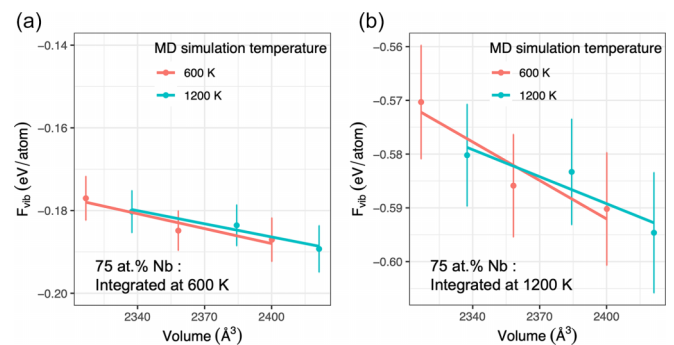
FIG. 9. F_{vib} calculated using $g(\omega)$ obtained from 600 K and 1200 K AIMD simulation, integrated at (a) 600 K and (b) 1200 K. The points show the mean value of F_{vib} calculated over 5 ps segments and the error bars show the standard deviations.
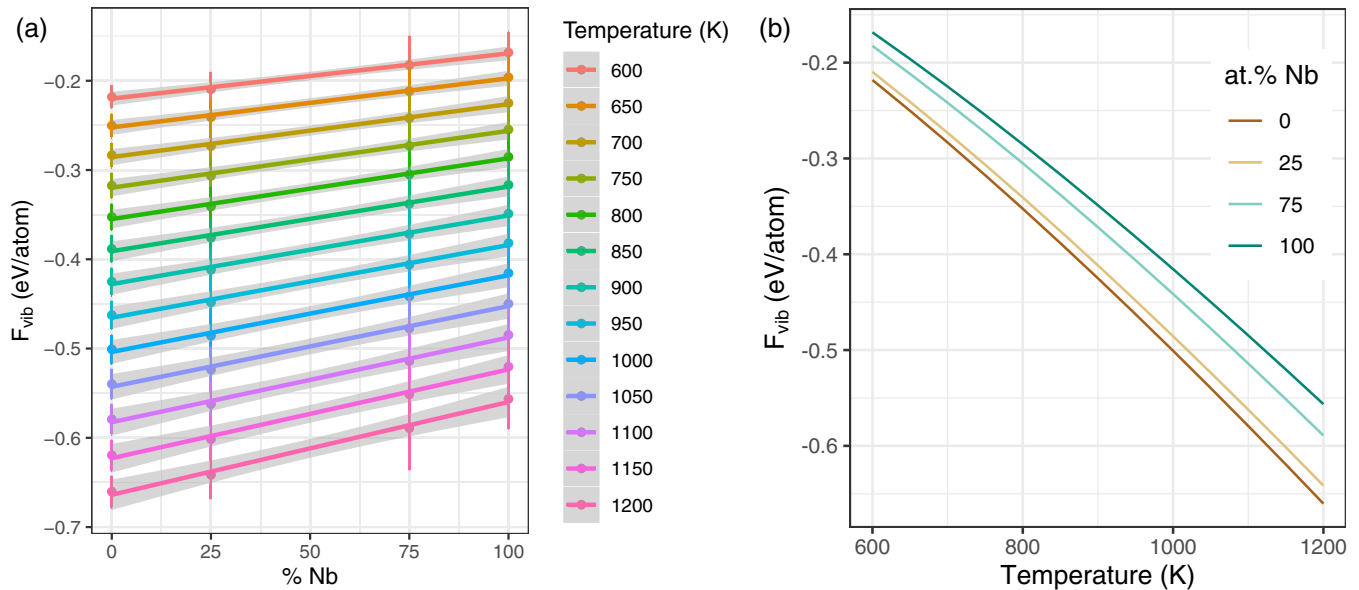
FIG. 10. Zero-pressure vibrational free energy of BCC-based phases as a function of (a) composition and (b) temperature. Linear regression added (a) with a confidence interval (shaded region) of 95%. Error bars in (a) are given by ϵ from Eq. (18).

perature. Thus, here we used $g(\omega)$ constructed from 600 K AIMD trajectories for all compositions except pure BCC-Zr, which displayed a phase transformation as outlined above. In the latter case, the AIMD $g(\omega)$ calculated at 1200 K was used instead.

In the range of volumes considered, and within the standard deviations of our data, the relationship between F_{vib} and V is described by a linear fit. Thus, the vibrational free energy at volume corresponding to zero-pressure is obtained, at any temperature, through a linear regression of F_{vib} with V to identify the intercept with V_0, the volume corresponding to zero-pressure at that temperature, identified from Fig. 6.

The vibrational free energy at zero pressure of β-(Zr,Nb) phases at any temperature was calculated from the $g(\omega)$. The zero-pressure volumes at any temperature can be calculated by accounting for the linear thermal expansion coefficient of BCC-Nb and BCC-Zr to get the respective lattice parameters at any temperatures. At all temperatures, the coefficient of thermal expansion for BCC-Nb and BCC-Zr were taken as 7.1×10^{-6} K^{-1} [72] and 10^{-5} K^{-1} [73] respectively. As a check, applying the experimentally observed thermal expansion coefficient to the lattice parameter obtained at 600 K for BCC-Nb in order to extrapolate this value to 1200 K and room temperature, results in lattice parameters of 3.343 Å and 3.326 Å respectively. These are in great agreement with the values supplied in Table I.

Figure 10(a) shows the vibrational free energy at zero-pressure of all four phases (BCC-Zr, BCC-Nb, β-Zr, and β-Nb) at multiple temperatures between 600 and 1200 K. The change in F_{vib} with composition appears to increase linearly with increasing Nb content, providing an estimate of F_{vib} at arbitrary compositions. It is observed that the 95% confidence interval of this linear regression fits inside the uncertainty of the data points at the four phases studied. As expected the zero-pressure vibrational free energy decreases with increasing temperature, see Fig. 10(b).

C. β-Zr decomposition reaction energy

With $F_{vib}(T)$ calculated for β-phase solid solutions and BCC-Nb, these values can be added along with $F_{elec}(T)$ to Eq. (2) to get the complete ΔG at zero pressure. $F_{elec}(T)$ was also calculated at all the temperatures probed for $F_{vib}(T)$. This time we calculate ΔG with respect to HCP-Zr and β-Nb to mimic the decomposition reaction of β-Zr. Considering a high-quality interatomic potential by Ackland *et al.* is available for HCP-Zr, $F_{vib}^{HCP-Zr}(T)$ has been obtained by running a classical MD simulation for 16 000 atoms supercell over 20 ps at 600 K and integrating the resultant $g(\omega)$ at temperatures of interest [74]. This is assumed to be an accurate depiction of the vibrational dynamics of HCP-Zr while reducing the computational cost, as the F_{vib} obtained for BCC-Zr through AIMD (120 atoms) and classical MD (16 000 atoms) at 1200 K are in excellent agreement, with values of–0.66 eV/atom and–0.65 eV/atom, respectively. It is worth noting that the same potential was used for both HCP and BCC-Zr [74] (see the Supplemental Material [47]).

Figure 11 shows ΔG for the decomposition reaction of β-Zr (25 at.% Nb) into HCP-Zr and β-Nb (75 at.% Nb) phase, as found in Zr-Nb alloys used in nuclear applications, calculated using Eq. (2). The results are also compared to results showing contribution of formation enthalpy, configurational entropy, and electronic free energy in order to gain a better understanding of the effect of vibrational free energy on the relative stability of these phases. This comparison shows us that ignoring the contributions of F_{vib}, our results predict the β-Zr phase decomposing at all temperatures. If the uncertainty associated with our calculations are accounted for, adding the contributions of F_{vib} makes the decomposition reaction thermodynamically unfavorable at temperatures above the monotectoid temperature (∼883 K), which is consistent with experimental observations of the β-Zr phase only being observed in alloys annealed above the monotectoid temperature. The results also show the importance of F_{vib} in explaining
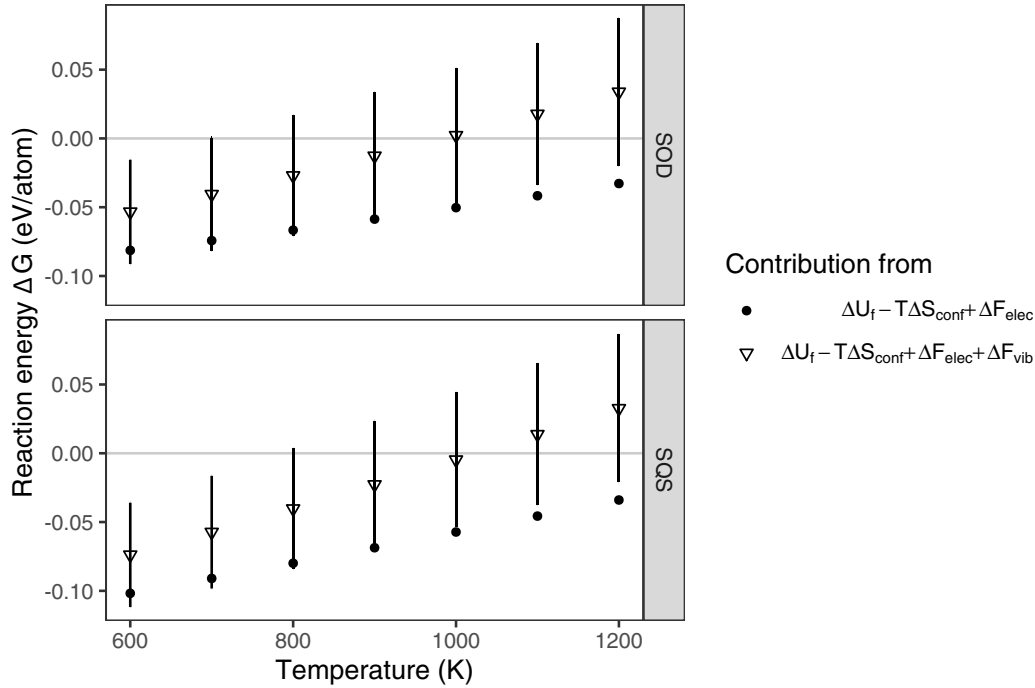
FIG. 11. ΔG for the β-Zr decomposition reaction between 600 and 1200 K. Error bars are calculated as $\sqrt{(\epsilon_{\beta\text{-Zr}}^2 + \epsilon_{\beta\text{-Nb}}^2)}$. HCP-Zr was not considered in the error propagation due to limited statistics obtained from classical MD run.

the decomposition of β-Zr at lower temperatures, but not above the monotectoid temperature. The energy of the decomposition reaction also increases with increasing temperature, showing that the chances of the β-phase decomposing reduces with increasing temperature.

IV. DISCUSSION

The thermodynamic stability of β-(Zr,Nb) phases was analyzed by first considering the contributions from ΔU_{mix} and configurational entropy. It is shown that, as expected with most metallic solid solution, the ΔU_{mix} is positive over most of the Zr/Nb compositional range. ΔU_{mix} values are in great agreement with the available literature as well. Adding the contribution of configurational entropy ($-T \Delta S_{\text{config}}$) lowered the overall energy of the β-(Zr,Nb) phases, but not sufficiently to explain the observed stability of β phases in Zr-Nb alloys.

ΔF_{elec} contributions were also considered while analyzing the thermodynamic stability of the β-(Zr,Nb) system. The contribution of ΔF_{elec} to ΔG was found to be quite small at lower temperatures with a difference of only 4% between ΔG and $\Delta G - \Delta F_{\text{elec}}$ values at 600 K. This difference increases to 39% at 1200 K. This observation is commensurate with prior literature suggesting that contribution of electronic free energy (relative to HCP-Zr) on the stability of BCC-Zr at high temperatures ($\sim$1000 K) cannot be ignored and that F_{elec} plays a bigger role than F_{vib} close to melting temperature [75].

The bulk of the work done here concentrated on using AIMD to calculate the contribution of ΔF_{vib} towards the relative thermodynamic stability of β-Zr and β-Nb. As shown in

the Supplemental Material [47], relatively small (120 atoms) anisotropic supercells were used to accurately capture the dynamics of the β-(Zr,Nb) system. This is verified by the accurate depiction of BCC-Zr instability at 600 K and capturing the effects of Nb as a beta-stabilizing agent. The excellent agreement between the available literature and simulated lattice parameters of pure BCC-Zr and BCC-Nb as well as β-(Zr,Nb) phases further validates the choice of supercell and AIMD simulation parameters. It is also shown that $g(\omega)$ obtained at a single temperature that is sufficiently high to stabilise the BCC structure can be used to obtain the vibrational free energies at a range of temperatures, further reducing the computational cost of these simulations.

When all major free-energy contributions and the relative uncertainty (0.05 eV at 600 K and 0.1 eV at 1200 K) are taken into account, the relative stability of β-Zr and β-Nb phases appear to be dictated by small energy changes, of the order of $\sim$0.1 eV/atom. The thermodynamics of the Zr-Nb system presented here might also explain the presence of differing compositions of β phases in Zr-Nb alloys. Since the difference in energies is so small, small differences in the microstructure, caused by thermomechanical processing or by radiation damage, could change the preferred composition of these β phases. This may explain the differences in β-phase composition observed between neutron and proton irradiated samples [22,23]. It has previously been reported that the difference in β-phase size and composition between neutron and proton irradiated samples may be attributed to the irradiation dose rate and diffusion kinetics [76,77]. Another possible reason could be the interaction of irradiation species with the sample. When proton irradiation causes small cascades, it impacts the process of steady state size stabilization of β phases due to

reordering caused by irradiation enhanced diffusion [77]. This might explain the formation of larger but less dense platelet-like precipitates [22,23].

The range of energies dictating the relative stability of these phases fall within the limit of accuracy of DFT. It is also likely that using classical MD on a 16 000 atom supercell, at the equilibrated 600 K volume (without accounting for thermal expansion), to approximate the vibrational free energy of HCP-Zr at multiple temperatures introduces a small error in the results. Another possible source of error is only sampling on the gamma-point in the reciprocal space due to computational constraints. Even though it is known that single gamma point sampling is good enough for big enough supercells [78,79], the accuracy level required in this case is quite high as the energies being analyzed are so small. It has been reported that a k-point density as high as 5000 k-points/Å^{-3} is typically required to obtain an accuracy of the total energy better than 1 meV per atom [80].

Work done here shows that the relative stability of these β phases can be explained by accounting for ΔH, $\text{T}\Delta S_{\text{conf}}$, ΔF_{elec}, and ΔF_{vib}. Other factors that may further lower the ΔG of β phases in Zr-Nb alloys must also be considered. These include, but are not limited to, effect of interfacial energy, impurities, and vacancies. While some irradiation induced nano-sized precipitates are coherent, the pre-irradiation β-Nb precipitates are often incoherent. Interfacial energy, at the interface of coherent/semicoherent β-Nb and β-Zr phase and bulk of the alloy, may also contribute towards the stability of β phases. Fe is both a common alloying element in Zr alloys and an impurity in Zr sponge. In binary Zr-Nb alloys, the concentration of Fe impurities is usually high ($\sim$1000 ppm). Fe is a β stabiliser, with limited solubility in HCP-Zr (50–80 ppm) and higher solubility in the β phase with native β-Nb SPPs in low-Sn Zirlo shown to contain about 1 wt% Fe [17,81,82]. These SPPs are also surrounded by a shell containing 6 wt% Fe, with reduction to 1 wt% Fe postirradiation [17,83]. Fe has also been reported to be present in the β-Zr phase [84]. Therefore, it is expected that further analysis of contribution of Fe inside or in the shell surround the native β-Nb phase will have an effect on the thermodynamic stability of these phases. Accounting for the Fe impurity effect may further lower the β-Zr decomposition reaction energy and increase the difference in energies between the values at 600 and 1200 K. Other common impurities include O and H, which are α and β stabilisers respectively. The concentration of these impurities will have an impact on the energy of the decomposition reaction as well.

The possible effect of vacancies on the stability of β phases must also be considered. MD studies have suggested that the vacancy formation energy in BCC-Zr is lower than in HCP-Zr ($\sim$1.6 eV vs 2.25 eV at 600 K) [85,86]. Moreover, in the temperature range of 1200–2200 K, previous calculations for equilibrium vacancy concentrations have shown that the equilibrium vacancy concentration is considerably higher in BCC-Zr and the vacancy concentration reduced more drastically in HCP-Zr than in BCC-Zr with decreasing temperature [85]. The coherent or semicoherent interfaces of the irradiation induced precipitates may lead to significant strain fields [18,22,87], which might be accommodated more easily with increasing vacancies (resulting in reduced bulk modulus) in

the β phases. It is worth noting that calculating the vacancy formation energy using DFT (at 0 K) is a formidable task since adding a vacancy in the BCC-Zr structure in DFT results in the entire structure collapsing as BCC-Zr is dynamically unstable at 0 K. The methodology presented here can be used to simulate the effect of an increasing number of vacancies in the β phases at the DFT level of theory by systematically introducing them in to the structures being simulated using AIMD. This will allow the approximation of the possibly significant impact of vacancies on the thermodynamic stability of β phases in Zr-Nb alloys.

V. CONCLUSIONS

This comprehensive analytical work done on the stability of β phases present in Nb-containing Zr alloys has resulted in a number of important findings. Results show that an accurate depiction of the dynamics of the β-(Zr,Nb) system can be obtained by running AIMD simulations for relatively small anisotropic structures. This is further verified by the accurate depiction of BCC-Zr instability at 600 K and capturing the effects of Nb as a beta-stabilizing agent. This finding of using small anisotropic cells is important as this makes AIMD simulations computationally feasible. It is also shown that $g(\omega)$ obtained at a single temperature high enough to stabilise the BCC structure can be used to obtain the vibrational free energies at a range of temperatures.

Within the uncertainty of the calculations, results presented here explain the experimental observation of the β-Zr phase in alloys annealed at higher temperatures, and vibrational entropy plays an important role in explaining these observations. Finally, the small difference in the ΔG between compositionally different β phases, of the order of $\sim$0.1 eV/atom, can explain the presence of wide range of compositions of these phases depending on manufacturing and irradiation conditions.

Other possible factors contributing towards the stability of β-(Zr,Nb) phases have also been discussed and these include presence of Fe as an impurity in Zr-Nb alloys, strains induced in the alloys due to β-phase precipitation, interfacial energy, and vacancies. Calculating the exact contributions of these factors towards the thermodynamics of the β-(Zr,Nb) system can form the foundation of future studies.

[1] T. Filburn and S. Bullard, *Three Mile Island, Chernobyl and Fukushima* (Springer, New York, 2016), pp. 105–114.

[2] G. P. Sabol, G. R. Kilp, M. G. Balfour, and E. Roberts, ASTM, Zirconium in the nuclear industry: Fifteenth international symposium, 227 (2008).

[3] G. Garner, B. Hilton, and E. Mader, in *2007 LWR Fuel Performance Meeting/TopFuel 2007 'Zero by 2010'* (American Nuclear Society, La Grange Park, IL, 2007)

[4] Y. H. Jeong, K. O. Lee, and H. G. Kim, J. Nucl. Mater. **302**, 9 (2002).

[5] B. B. Straumal, A. S. Gornakova, O. B. Fabrichnaya, M. J. Kriegel, A. A. Mazilkin, B. Baretzky, A. Gusak, and S. Dobatkin, High Temp. Mater. Processes (London) **31**, 339 (2012).

[6] J. Y. Park, B. K. Choi, Y. H. Jeong, and Y. H. Jung, J. Nucl. Mater. **340**, 237 (2005).

[7] S. Banerjee, S. J. Vijayakar, and R. Krishnan, J. Nucl. Mater. **62**, 229 (1976).

[8] G. He, J. Liu, K. Li, J. Hu, A. H. Mir, S. Lozano-Perez, and C. Grovenor, J. Nucl. Mater. **526**, 151738 (2019).

[9] S. Doriot, B. Verhaeghe, J. L. Béchade, D. Menut, D. Gilbon, J. P. Mardon, J. M. Cloué, A. Miquet, and L. Legras, in Zirconium in the nuclear industry: 17th International Symposium **STP 1543**, 759 (2015).

[10] B. D. Warr, M. B. Elmoselhi, S. B. Newcomb, N. S. McIntyre, A. M. Brennenstuhl, and P. C. Lichtenberger, in Zirconium in the nuclear industry: Ninth International Symposium **1132**, 740 (1991).

[11] A. Perovic, V. Perovic, G. G. Weatherly, G. R. Purdy, and R. G. Fleck, J. Nucl. Mater. **199**, 102 (1993).

[12] H. G. Kim, S. Y. Park, M. H. Lee, Y. H. Jeong, and S. D. Kim, J. Nucl. Mater. **373**, 429 (2008).

[13] V. Perovic, A. Perovic, G. Weatherly, and G. Purdy, J. Nucl. Mater. **224**, 93 (1995).

[14] C. Cann, C. So, R. Styles, and C. Coleman, J. Nucl. Mater. **205**, 267 (1993).

[15] H.-G. Kim, B.-K. Choi, S.-Y. Park, Y.-I. Jung, D.-J. Park, and J.-Y. Park, J. Nucl. Mater. **426**, 173 (2012).

[16] V. Shishov, M. Peregud, A. Nikulina, V. Kon'Kov, V. Novikov, V. Markelov, T. Khokhunova, G. Kobylyansky, A. Novoselov, Z. Ostrovsky *et al.*, J. ASTM Int. **5**, 101127 (2008).

[17] E. Francis, A. Harte, P. Frankel, S. Haigh, D. Jädernäs, J. Romero, L. Hallstadius, and M. Preuss, J. Nucl. Mater. **454**, 387 (2014).

[18] J. Ribis, S. Doriot, and F. Onimus, J. Nucl. Mater. **511**, 18 (2018).

[19] C. E. Coleman, R. W. Gilbert, G. J. C. Carpenter, and G. C. Weatherly, in *Phase Stability During Irradiation*, edited by J. R. Holland, L. K. Mansur, and D. I. Potter (Metallurgical Society of AIME, New York, 1981), pp. 587–599.

[20] V. Shishov, M. Peregud, A. Nikulina, Y. Pimenov, G. Kobylyansky, A. Novoselov, Z. Ostrovsky, and A. Obukhov, J. ASTM Int. **2**, 12431 (2005).

[21] S. Doriot, B. Verhaeghe, A. Soniak-Defresne, P. Bossis, D. Gilbon, V. Chabretou, J.-P. Mardon, M. Ton-That, and A. Ambard, in *Zirconium in the Nuclear Industry: 18th International Symposium* (ASTM International, West Conshohocken, PA, 2018).

[22] Z. Yu, C. Zhang, P. M. Voyles, L. He, X. Liu, K. Nygren, and A. Couet, Acta Mater. **178**, 228 (2019).

[23] Z. Yu, A. Couet, and M. Bachhav, J. Nucl. Mater. **516**, 100 (2019).

[24] M. Cottura and E. Clouet, Acta Mater. **144**, 21 (2018).

[25] Y. Zhao, H. Li, and Y. Huang, J. Alloys Compd. **862**, 158029 (2021).

[26] O. Hellman, I. A. Abrikosov, and S. I. Simak, Phys. Rev. B **84**, 180301(R) (2011).

[27] V. Y. Trubitsin and E. B. Dolgusheva, Phys. Rev. B **76**, 024308 (2007).

[28] A. Gupta, B. Tas, D. Korbmacher, D. Butta, Y. Neitzel, B. Grabowski, T. Hickel, V. Esin, S. V. Divinski, G. Wilde *et al.*, Materials **14**, 1837 (2021).

[29] M. Palumbo, S. G. Fries, A. Pasturel, and D. Alfè, J. Chem. Phys. **140**, 144502 (2014).

[30] Y. Cui, X. Chen, C. Li, L. Liu, D. Zhang, J. Li, Y. Tang, and H. Tian, Chem. Phys. Lett. **780**, 138961 (2021).

[31] B. Grabowski, L. Ismer, T. Hickel, and J. Neugebauer, Phys. Rev. B **79**, 134106 (2009).

[32] M. D. Hossain, T. Borman, C. Oses, M. Esters, C. Toher, L. Feng, A. Kumar, W. G. Fahrenholtz, S. Curtarolo, D. Brenner *et al.*, Adv. Mater. **33**, 2102904 (2021).

[33] A. Manzoor, S. Pandey, D. Chakraborty, S. R. Phillpot, and D. S. Aidhy, npj Comput. Mater. **4**, 47 (2018).

[34] L. Fan, C. Shen, K. Hu, H. Liu, and H. Zhang, J. Phase Equilib. Diffus. **42**, 348 (2021).

[35] Y. Wang, K. Li, F. Soisson, and C. S. Becquart, Phys. Rev. Mater. **4**, 113801 (2020).

[36] E. Martínez, O. Senninger, C.-C. Fu, and F. Soisson, Phys. Rev. B **86**, 224109 (2012).

[37] M. Ozawa, G. Parisi, and L. Berthier, J. Chem. Phys. **149**, 154501 (2018).

[38] A. van de Walle, P. Tiwary, M. De Jong, D. L. Olmsted, M. Asta, A. Dick, D. Shin, Y. Wang, L. Q. Chen, and Z. K. Liu, Calphad **42**, 13 (2013).

[39] R. Grau-Crespo, S. Hamad, C. R. A. Catlow, and N. De Leeuw, J. Phys.: Condens. Matter **19**, 256201 (2007).

[40] G. Kresse and J. Furthmuller, Comput. Mater. Sci. **6**, 15 (1996).

[41] G. Kresse and J. Furthmuller, Phys. Rev. B **54**, 11169 (1996).

[42] E. Hecht, *Optics* (Addison-Wesley, Reading, MA, 2002).

[43] N. Shulumba, B. Alling, O. Hellman, E. Mozafari, P. Steneteg, M. Odén, and I. A. Abrikosov, Phys. Rev. B **89**, 174108 (2014).

[44] R. G. Della Valle, E. Venuti, and A. Brillante, Gazz. Chim. Ital. **126**, 615 (1996).

[45] Á. Cimas, F. Tielens, M. Sulpizi, M.-P. Gaigeot, and D. Costa, J. Phys.: Condens. Matter **26**, 244106 (2014).

[46] Y. Shi, M. Liu, J. Wang, H. Ma, R. Li, Y. Chen, W. Mo, D. Li, B. Bai, X. Wang *et al.*, Nucl. Mater. Energy **26**, 100915 (2021).

[47] See Supplemental Material at http://link.aps.org/supplemental/10.1103/PhysRevMaterials.7.113607 for AIMD parameter convergence and Helmholtz vibrational free energy between 50 K and 1200 K for all volumes simulated using AIMD.

[48] G. Paglia, A. L. Rohl, C. E. Buckley, and J. D. Gale, Phys. Rev. B **71**, 224115 (2005).

[49] J. H. Rose, J. R. Smith, F. Guinea, and J. Ferrante, Phys. Rev. B **29**, 2963 (1984).

[50] O. Jin, Z. Zhang, and B. Liu, J. Appl. Phys. **78**, 149 (1995).

[51] N. Al-Aqeeli, M. A. Hussein, and C. Suryanarayana, Adv. Powder Technol. **26**, 385 (2015).

[52] H. Y. Bai, C. Michaelson, C. Gente, and R. Bormann, Phys. Rev. B **63**, 064202 (2001).

[53] S. Zhang, K. Khor, and L. Lü, J. Mater. Process. Technol. **48**, 779 (1995).

[54] S. Kumar and V. Jindal, J. Phase Equilib. Diffus. **43**, 511 (2022).

[55] B. Fultz, Prog. Mater. Sci. **55**, 247 (2010).

[56] Z.-G. Mei, S.-L. Shang, Y. Wang, and Z.-K. Liu, Phys. Rev. B **80**, 104116 (2009).

[57] A. Togo and I. Tanaka, Scr. Mater. **108**, 1 (2015).

[58] W. G. Hoover, Phys. Rev. A **31**, 1695 (1985).

[59] P. Vinet, J. R. Smith, J. Ferrante, and J. H. Rose, Phys. Rev. B **35**, 1945 (1987).

[60] M. R. Fellinger, H. Park, and J. W. Wilkins, Phys. Rev. B **81**, 144119 (2010).

[61] K. Yan, D. G. Carr, S. Kabra, M. Reid, A. Studer, R. P. Harrison, R. Dippenaar, and K.-D. Liss, Adv. Eng. Mater. **13**, 882 (2011).

[62] G. Aurelio, A. F. Guillermet, G. Cuello, and J. Campo, Metall. Mater. Trans. A **34**, 2771 (2003).

[63] A. Heiming, W. Petry, J. Trampenau, W. Miekeley, and J. Cockcroft, J. Phys.: Condens. Matter **4**, 727 (1992).

[64] J. Tidholm, O. Hellman, N. Shulumba, S. I. Simak, F. Tasnádi, and I. A. Abrikosov, Phys. Rev. B **101**, 115119 (2020).

[65] H. Goldschmidt, J. Iron Steel Inst. **194**, 169 (1960).

[66] P. M. Larsen, arXiv:2003.08879.

[67] D. Smirnova, S. Starikov, and I. Gordeev, Comput. Mater. Sci. **152**, 51 (2018).

[68] D. Hayes and F. Brotzen, J. Appl. Phys. **45**, 1721 (1974).

[69] X. Chen, D. Wang, B. Yao, L. Wu, X. Wu, and Y. Wang, J. Nucl. Mater. **568**, 153876 (2022).

[70] A. Masago, K. Shirai, and H. Katayama-Yoshida, Phys. Rev. B **73**, 104102 (2006).

[71] L.-F. Huang and Z. Zeng, J. Phys. Chem. C **119**, 18779 (2015).

[72] S. Y. Betsofen, A. A. Lozovan, A. S. Lenkovets, A. A. Labutin, and I. A. Grushin, Russ. Metall. (Metally) **2021**, 883 (2021).

[73] D. E. Smirnova and S. V. Starikov, Comput. Mater. Sci. **129**, 259 (2017).

[74] M. I. Mendelev and G. J. Ackland, Philos. Mag. Lett. **87**, 349 (2007).

[75] E. G. Moroni, G. Grimvall, and T. Jarlborg, Phys. Rev. Lett. **76**, 2758 (1996).

[76] G. S. Was, J. Mater. Res. **30**, 1158 (2015).

[77] G. S. Was, *Fundamentals of Radiation Materials Science: Metals and Alloys* (Springer, New York, 2016).

[78] M. Valter, B. Wickman, and A. Hellman, J. Phys. Chem. C **125**, 1355 (2021).

[79] X. Hu, S. Yao, L. Chen, X. Zhang, M. Jiao, Z. Lu, and Z. Zhou, J. Mater. Chem. A **9**, 23515 (2021).

[80] J. Moreno and J. M. Soler, Phys. Rev. B **45**, 13891 (1992).

[81] H. Zou, G. Hood, J. Roy, R. Packwood, and V. Weatherall, J. Nucl. Mater. **208**, 159 (1994).

[82] M. Griffiths, J. Nucl. Mater. **159**, 190 (1988).

[83] S. Huang, L. Tegg, J. Qu, L. Yang, I. McCarroll, P. A. Burr, and J. M. Cairney, Microscopy and Microanalysis **29**, 614 (2023).

[84] A. Harte, M. Griffiths, and M. Preuss, J. Nucl. Mater. **505**, 227 (2018).

[85] M. I. Mendelev and B. S. Bokstein, Philos. Mag. **90**, 637 (2010).

[86] F. Willaime and C. Massobrio, Phys. Rev. B **43**, 11653 (1991).

[87] A. A. Turkin, A. V. Buts, and A. S. Bakai, J. Nucl. Mater. **305**, 134 (2002).